

## HUBBLE SPACE TELESCOPE NICMOS SPECTROSCOPY OF CHARON'S LEADING AND TRAILING HEMISPHERES

CHRISTOPHE DUMAS AND RICHARD J. TERRILE

Jet Propulsion Laboratory, Mail Stop 183-501, California Institute of Technology, 4800 Oak Grove Drive, Pasadena, CA 91109

ROBERT H. BROWN

Lunar and Planetary Laboratory, University of Arizona, 1629 East University Boulevard, Tucson, AZ 85721

GLENN SCHNEIDER

Steward Observatory, University of Arizona, 933 North Cherry Avenue, Tucson, AZ 85721

AND

BRADFORD A. SMITH

Institute for Astronomy, University of Hawaii, 2680 Woodlawn Drive, Honolulu, HI 96822

Received 2000 August 1; accepted 2000 November 6

### ABSTRACT

We used the near-infrared camera and multiobject spectrometer NICMOS on the *Hubble Space Telescope* to obtain 1.1–2.4  $\mu\text{m}$ , low-resolution ( $R \sim 200$ ) slitless grism spectrophotometry of the individual members of the Pluto-Charon system. Water ice is present in its crystalline state on both the leading and trailing hemispheres of Charon. A 2.21  $\mu\text{m}$  absorption band, possibly due to the presence of ammonia hydrate in surface, is detected in the reflectance spectrum of its leading side only. Geological activity on Charon or implantation of ions escaped from Pluto's atmosphere could account for the formation of species such as  $\text{NH}_3 \cdot \text{H}_2\text{O}$  locally on the satellite. We also measured a slightly higher geometric albedo for Charon than reported from the mid-1980s observations of the mutual events.

*Key words:* planets and satellites: individual (Charon) — techniques: spectroscopic

### 1. INTRODUCTION

Although Pluto's discovery was made 70 years ago, most of the information we have collected on its surface composition has been obtained only very recently. Sensitive telescope instrumentation is now available to carry out spectrophotometric observations of the Pluto-Charon system at visible and, particularly, at near-infrared wavelengths, a spectral range that provides an excellent diagnostic of the physical state of the ices present on the surface. The surface of Pluto was first suggested to be primarily covered with methane ice (Cruikshank, Pilcher, & Morrison 1976). Additional photometric observations, carried out at various rotational phases (Buie & Fink 1987), showed that methane is not distributed uniformly over the surface. Owen et al. (1993) reported that  $\text{N}_2$  ice is in fact the most abundant compound on Pluto, followed by  $\text{CH}_4$  and  $\text{CO}$ . Currently, the planet is moving away from the Sun and its atmosphere is slowly condensing on the surface (Stern, Trafton, & Gladstone 1988). While  $\text{N}_2$  gas should also be the main constituent of Pluto's atmosphere (Owen et al. 1993), only methane gas has already been detected, from the  $2\nu_3$  band at 1.67  $\mu\text{m}$  (Young et al. 1997), and  $\text{CO}$  gas awaits detection. Pluto's surface displays patches of bright  $\text{N}_2$ -rich regions and dark nitrogen-depleted areas (Jewitt 1994).  $\text{N}_2$  ice may be concentrated in the polar regions at temperatures  $\leq 40$  K (Tryka et al. 1994), while ices with lower volatility should cover the equatorial regions. The surface temperature varies locally, and recent *Infrared Space Observatory* measurements (Lellouch et al. 2000) confirmed the presence of cold-bright regions and warm-dark regions. The visible albedo distribution across Pluto was determined from light-curve inversion techniques (Buie, Tholen, &

Horne 1992; Young et al. 1999) and direct imaging using the *Hubble Space Telescope* (*HST*) Faint Object Camera (Stern, Buie, & Trafton 1997). Both methods confirmed the presence of bright polar regions, while the equatorial zone displays a darker but highly variegated surface.

Because of the small angular separation between Pluto and its satellite (from 0'3 to 0'9), our knowledge of Charon's surface composition could, until recently, only be deduced from the analysis of the mid-1980s occultation events. These observations showed that Charon is mostly covered with  $\text{H}_2\text{O}$  ice (Buie et al. 1987; Marcialis, Rieke, & Lebofsky 1987; Fink & DiSanti 1988). Later analysis by Roush (1994) and Roush et al. (1996) of the mid-1980s photometric measurements suggested that the surface of Charon could also be covered with patches of  $\text{CO}_2$  ice mixed with large-grained  $\text{CH}_4$  ice in addition to  $\text{H}_2\text{O}$ . Dumas et al. (1999) reported *HST* Near Infrared Camera and Multi-Object Spectrometer (NICMOS) observations revealing for the first time the crystalline state of water ice over Charon. This result was confirmed by independent NICMOS observations of Charon made by Buie & Grundy (2000), as well as by ground-based observations carried out at Keck Observatory by Brown & Calvin (2000). Brown & Calvin also reported the presence of a 2.21  $\mu\text{m}$  band in their spectrum of Charon, which they attributed to the presence of ammonia ice on the surface.

This paper presents the results of a reanalysis of the *HST* NICMOS observations obtained by Dumas et al. (1999). We confirm the presence of a 2.21  $\mu\text{m}$  absorption feature in the spectrum of Charon; however, this absorption appears to be detected only in the spectrum of the leading hemisphere. This result suggests that resurfacing processes, pos-

TABLE 1  
GEOMETRY OF THE PLUTO-CHARON SYSTEM DURING THE 1998 JUNE “CAMERA 3 CAMPAIGN”

Property	Jun 11, UT 1301 <sup>a</sup>	Jun 14, UT 1456 <sup>a</sup>
Heliocentric distance (AU).....	30.0684	30.0692
Geocentric distance (AU).....	29.1049	29.1190
Sub-Earth latitude (deg).....	-21.4	-21.3
Pluto’s sub-Earth longitude (deg).....	99.6 (max. light curve)	273.2 (min. light curve)
Charon’s sub-Earth longitude (deg).....	279.7 (trailing side)	93.2 (leading side)
Separation (arcsec).....	0.908	0.917
Charon’s position angle (deg).....	169.95	347.65
Spectral separation (pixels).....	2.55 (=0’517)	2.70 (=0’548)

<sup>a</sup> Time at beginning of G206 series.

sibly involving Pluto, are currently occurring on Charon. A mechanism is discussed that involves bombardment of Charon’s surface by ions escaping from Pluto’s atmosphere.

## 2. OBSERVATIONS

We report spectroscopic observations of the Pluto-Charon system obtained in 1998 on June 11 and 14 (*HST* program GTO 7223) at Charon’s maximum elongation using *HST* and its near-infrared camera and multiobject spectrometer NICMOS (Thompson et al. 1998). The details of the geometry of the Pluto-Charon system are described in Table 1. Planetocentric coordinates were calculated for both dates using the 1994 IAU model (Davies et al. 1995).

NICMOS has three  $256 \times 256$  HgCdTe low-noise detectors covering a 0.8–2.4  $\mu\text{m}$  spectral range with pixel scales ranging from 43 mas pixel<sup>-1</sup> (camera 1) to 203 mas pixel<sup>-1</sup> (camera 3). Camera 3 (NIC3) is equipped with a set of three gratings, an optical setup combining a prism and a grating, providing low-resolution ( $R \sim 200$ ) slitless spectrophotometric capabilities. In this paper, we discuss the results obtained using NIC3 and the G141 and G206 gratings, spanning a spectral range from 1.1 to 2.4  $\mu\text{m}$ . Though NIC3 normally produces slightly afocal images, our data were obtained during the 1998 June “camera 3 campaign,” during which *HST*’s secondary mirror was adjusted to achieve optimal optical performance. Pluto and Charon were separated by 0’9 for the dates of our observations. However, because of *HST* scheduling constraints, the line joining the binary system could not be oriented perpendicular to the dispersion direction; hence, the spatial separation of the spectra was reduced to 0’5 (Table 1). Table 2 summarizes the exposure parameters for the G141 and G206 gratings. Because the wavelength solution of each spectrum is a function of the position of the science target on the detector, we initially obtained an image of Pluto-Charon through the F150W broad filter. Two spectra of Pluto-Charon (320 s per exposure) were then recorded with the G141 grism. A small telescope offset was implemented between each exposure to collect data from different locations on the detector and to reduce the contamination of

our data from flat-field residual effects, as well as to sample around bad pixels. The last step was to acquire the long-wavelength spectra using the G206 grism. Because the G206 background level was  $\sim 150$  times higher than for the G141 grism, shorter exposures were required in order to avoid saturation. We recorded a series of 12 spectra (64 s each) at four different locations on the detector (three images per position of the telescope).

## 3. DATA REDUCTION

The extraction and absolute photometric calibration of the spectra of Pluto and Charon were achieved using the “NICMOSlook” software (Pirzkal & Freudling 1998; McCarthy et al. 1999), developed at the Space Telescope European Coordinating Facility for reduction of the NICMOS spectroscopic data.

### 3.1. Separation of Pluto and Charon

The first step in data reduction was to subtract the background from the G206 images. The background was estimated from a median combination of the set of four-position dithered G206 images. The low background level for the G141 grism was simply fitted during the extraction. Because the spectra of the two objects partially overlap, we estimated their individual contributions and created, for each original spectrum, two images containing separate synthetic spectra of Pluto and Charon. Figure 1 shows the result of fitting the contribution of Pluto and Charon along one detector column. Because the 0’2 pixel<sup>-1</sup> scale of NIC3 oversamples the point-spread function (PSF), each image was first rebinned to a finer grid (rebin factor = 8) via bicubic convolution interpolation (Park & Schowengerdt 1983). The angle of dispersion of the spectra with respect to the detector’s horizontal axis was measured, as well as the location where the spectrum was illuminating the exact center of one pixel. From the knowledge of these two parameters, we could estimate the width of Pluto’s and Charon’s PSFs. The separated synthetic spectra of Pluto and Charon were obtained by adjusting the amplitude and position of the two PSFs in order to minimize the variance of the difference between the original and the synthetic profiles (Fig. 1). This measurement was made over the range of pixels covered by the two objects, and a good fit was reached after only three iterations. The process returned two images corresponding to the separated spectra of Charon and Pluto, which were rebinned back to the original resolution. The maximum count rate for Pluto in a single G206 exposure was near  $330 e^- s^{-1}$ , while the residual count rate was in the  $\pm 13 e^- s^{-1}$  range (NIC3 gain =  $6.5 e^- \text{ADU}^{-1}$ ). The residual image (original image

TABLE 2  
GRISM OBSERVATION PARAMETERS

Parameter	G141	G206
Spectral coverage ( $\mu\text{m}$ ).....	1.1–1.9	1.4–2.5
Number of exposures.....	2	12
Total exposure time (s).....	639.9	767.4
NICMOS sequence.....	STEP64	STEP16

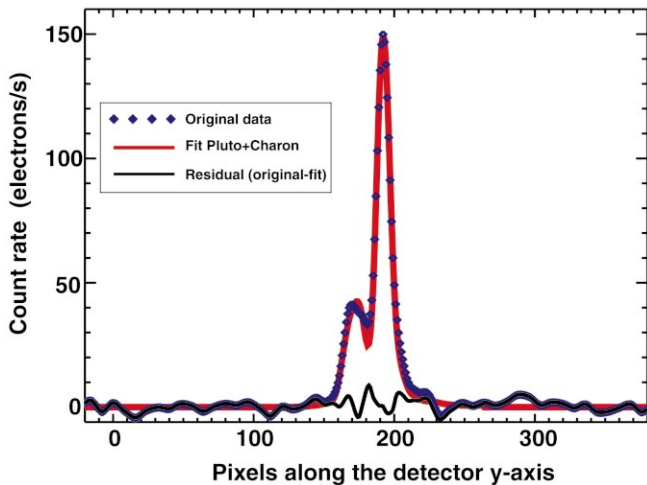


FIG. 1.—Cross section of a rebinned G206 spectrum of Pluto-Charon along the spatial direction ( $y$ -axis of the detector). The original profile is noted with diamonds, while the synthetic profile of Pluto plus Charon is indicated by the red line. The residual of the fit (original profile minus synthetic) is represented with a black line. For each original image, two synthetic images are produced by fitting the individual contributions of Pluto and Charon along the detector columns (three iterations of the fitting algorithm). The synthetic images are then used to extract the individual spectra of Pluto and Charon.

minus synthetic) was used to improve the models of Pluto’s and Charon’s spectra. The total flux  $\mathcal{F}_T$  in a detector pixel due to Pluto ( $\mathcal{F}_P$ ) and Charon ( $\mathcal{F}_C$ ) is simply  $\mathcal{F}_T = \mathcal{F}_P + \mathcal{F}_C$ , and the residual value for one particular pixel is  $\text{res} = \mathcal{F}_{\text{orig}} - \mathcal{F}_T$ , where  $\mathcal{F}_{\text{orig}}$  is the flux of the original image for this pixel. Then the corrected fluxes for the fits of Pluto and Charon are respectively  $F'_P = F_P + (F_P/F_T)\text{res}$  and  $F'_C = F_C + (F_C/F_T)\text{res}$ . This correction, performed individually for all pixels, allows us to conserve the original total flux of Pluto and Charon while correcting the models for the uncertainties in the individual pixel response and the exact position of the PSF with respect to the center of the pixel.

### 3.2. Extraction of the Spectra

At this stage, the data have been processed in such a way that we can extract and photometrically calibrate the G141 and G206 spectra of Pluto and Charon. Version 2.9.2 of NICMOSlook (Freudling & Pirzkal 1998; Pirzkal & Freudling 1998) was used for this purpose. The wavelength solution for all NICMOS grisms as a function of the position of the object on the detector has been parameterized. The only adjustment we made consisted of accounting for the planet’s apparent motion, which had the effect of modifying the original position measured from the F150W image. The NICMOS detectors do not have spatially flat responses across their pixels. Thus, the flux measured in an undersampled pixel depends upon the location of the PSF core with respect to the pixel center. It was therefore necessary to extract the spectra using a model of the intrapixel response function (IPRF; see Lauer 1999 for a detailed description). The average effect of the IPRF was larger for “camera 3 campaign” observations than for observations carried out when the PSF was not exactly in focus for NIC3. Similarly, because the PSF is better sampled at longer wavelengths, the correction for the G206 grism data was smaller than for the G141 grism. We used the obser-

vations of the solar analog P330-E collected during the 1998 June “camera 3 campaign” (*HST* program 7959) to determine the amplitude of a characteristic IPRF correction to apply to our G206 and G141 spectra. The scatter of the data points was measured before and after applying the IPRF correction. For this purpose, we defined the mean spectrum for each grism and subtracted it from the individual spectra to calculate the means of the standard deviations over a defined range of wavelengths. After applying the IPRF, we measured a decrease in the means of the standard deviations of 10% and 40%, respectively, for the G206 and G141 grisms.

### 3.3. Calibration

#### 3.3.1. Spectral Calibration

Given that the wavelength solution for each spectrum is a function of the target location on the detector, the estimation of this location (from the F150W image and the apparent motion of the object) provides an additional source of error for the spectral calibration. The wavelength sampling of the spectra after extraction is  $10 \text{ nm pixel}^{-1}$  (G206 grism). Therefore we first rebinned the individual spectra to a finer grid prior to co-registering them (this process was similarly applied to the spectrum of the solar analog P330-E). The spectra of P330-E and Pluto-Charon were then co-registered, using the absorption bands visible in both spectra as fiducial. Because of the lower signal-to-noise ratio (S/N) of the G206 data, and the deep bands of methane and water present at these wavelengths, the co-registration process returned a less accurate wavelength calibration for the G206 grism than for G141. The accuracy of the wavelength calibration of the spectra is of the order of 20 nm for the G206 grism, slightly better at shorter wavelengths (G141 grism). This is illustrated by the small shifts ( $\leq 20 \text{ nm}$ ) in wavelength that can be measured for the  $1.85 \mu\text{m}$  band of methane and the  $2.05 \mu\text{m}$  band of water in Figure 2. Smaller wavelength shifts can also be noticed for the G141 grism. Such shifts result from the uncertainty in the wavelength calibration of our data set and do not represent any real hemispheric variations in the physical state of the surface ices.

#### 3.3.2. Radiometric Calibration

For each pixel, the response function in wavelength used to flat-field the spectra was determined by interpolating the narrowband flat fields ( $\Delta\lambda/\lambda \sim 1\%$ ) obtained as part of the standard NICMOS Cycle 7 calibration program. The inverse sensitivity curves (used by NICMOSlook to convert the spectral flux into millijanskys) were obtained for each grism from observations of the calibrator stars P330-E and G191-B2B collected during the 1998 June “camera 3 campaign.” The intensities of the individual G206 spectra were adjusted to minimize the scatter in our data set, and the  $1 \sigma$  errors represent the residual dispersion after correction. Comparison of the G141 and G206 spectra shows a mismatch in the overlap region, and we estimate the G206 flux to be 12% higher than the G141 flux after calibration. Using recent ground-based observations of Pluto carried out by Owen et al. (1993) and recalibrated in geometric albedo by Roush et al. (1996), we find that the G141 grism calibration is best matched by the ground-based results, giving geometric albedos of  $p \sim 0.55$  and  $p \sim 0.7$  at  $1.9 \mu\text{m}$  for the minimum and maximum of Pluto’s light curve, respectively. The precision of the flux calibration returned

by the G141 grism is higher because its lower background makes the extraction of the photometric calibrators more accurate. We therefore selected the G141 grism as the reference for our photometric calibration. Our spectra of Pluto and Charon were then divided by the spectra of the solar analog P330-E (which were extracted using NICMOSlook as described above). After correction of our spectra for the solar spectrum, we calibrated the spectra of Pluto and Charon in geometric albedo using the solar flux given by Labs & Neckel (1968) and the radii for Pluto ( $1151 \pm 4$  km) and Charon ( $591 \pm 5$  km) determined by Reinsch, Burwitz, & Festou (1994). An independent reference for the solar flux (Thekekar 1973) was used and returned the same calibration values.

#### 4. RESULTS AND DISCUSSION

Figure 2 shows the calibrated NICMOS spectra of Pluto and Charon obtained for the two dates 1998 June 11 and 14. The spectra have been slightly smoothed (convolution with a 2 pixel wide Gaussian) in this figure in order to make their comparison easier. The original spectra with error bars are presented below, along with the modeling results in § 4.2.2.

##### 4.1. Pluto

The focus of this paper being Charon, we will not provide a detailed model and discussion for the case of Pluto (Fig. 2a) and will refer to Douté et al. (1999) for recent modeling of Pluto's spectra. Nevertheless, we will note, as a proof of the validity of the extraction procedure described above, that (1) the two grism spectra are self-consistent in the 1.60–1.85  $\mu\text{m}$  overlap region and (2) there is excellent agreement between our NICMOS spectra and the higher resolution spectra obtained by Douté et al. (1999). The strong bands of methane ice are clearly visible, as well as the 2.15  $\mu\text{m}$  dip due to  $\text{N}_2$ , particularly for the spectrum that corresponds to minimum of Pluto's light curve. Comparison of our spectra at both light-curve minimum and maximum with the higher resolution ground-based spectra obtained at UKIRT by Cruikshank et al. (1997) also shows an excellent agreement between the two data sets for the 1.9  $\mu\text{m}$  "continuum" region. At shorter wavelengths, we note that our determination of Pluto's albedo is slightly higher than that reported by the UKIRT measurements, but comparison of the relative 1.22  $\mu\text{m}$ /1.9  $\mu\text{m}$  ratio of the  $\text{CH}_4$  continuum between our calibrated NICMOS spectra and recent ground-based data obtained at Keck (Brown & Calvin 2000) confirms that the continuum level for the blue end of the spectra is higher

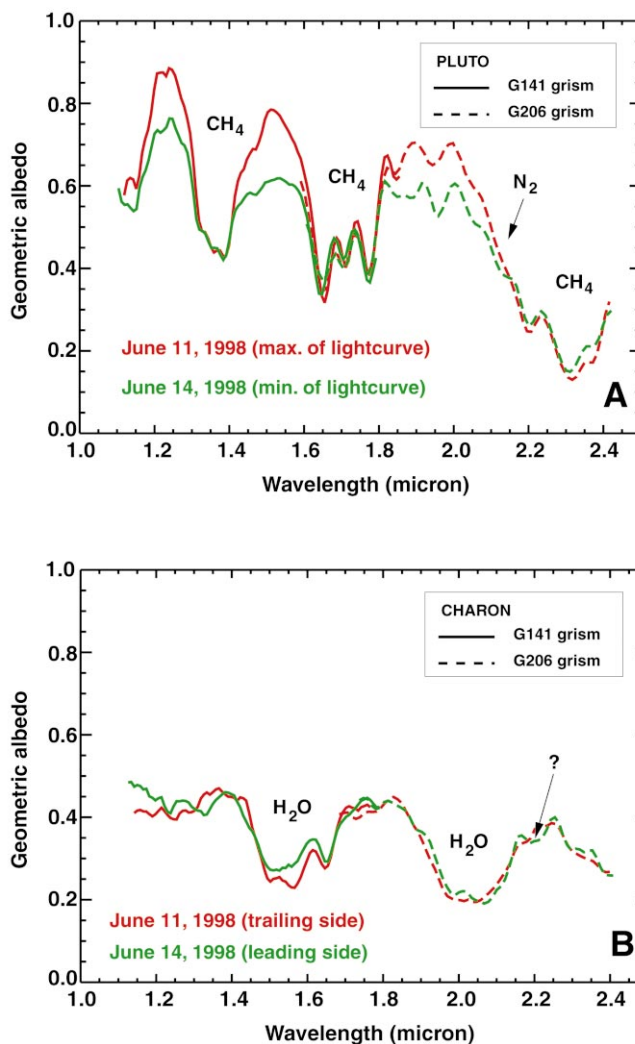


FIG. 2.—G141 and G206 spectra of (a) Pluto and (b) Charon obtained during the “camera 3 campaign” of 1998 June. The species responsible for the absorption bands detected in our spectra are noted on the figures. Near-infrared spectroscopy of Charon shows that the 1.65  $\mu\text{m}$  feature of crystalline water ice is visible for both the leading and trailing sides. The 2.21  $\mu\text{m}$  absorption reported from Keck observations of Charon by Brown & Calvin (2000) is visible in the *HST* NICMOS spectrum, but for the leading hemisphere only. Whatever compound ( $\text{NH}_3$ ?) is responsible for this absorption, it is more abundant on the leading side of the satellite than on its trailing side.

than previously reported. Additional discussion about the flux calibration of our NICMOS data is presented in § 4.2.2. Table 3 presents the broadband photometric measurements derived from our spectroscopic data set for both obser-

TABLE 3  
NEAR-INFRARED PHOTOMETRY OF PLUTO-CHARON

DATE (1998)	PLUTO (mag)			CHARON (mag)		
	$J^a$	$H^b$	$K^c$	$J^a$	$H^b$	$K^c$
Jun 11 .....	$12.69 \pm 0.01$	$12.66 \pm 0.01$	$13.09 \pm 0.04$	$14.74 \pm 0.03$	$14.70 \pm 0.02$	$14.81 \pm 0.12$
Jun 14 .....	$12.83 \pm 0.02$	$12.81 \pm 0.02$	$13.19 \pm 0.04$	$14.70 \pm 0.04$	$14.63 \pm 0.04$	$14.81 \pm 0.10$

NOTE.—These measurements are derived from the spectra in Fig. 3. The error bars in magnitude reflect only the  $1\sigma$  uncertainty plotted in the figure. The absolute photometric accuracy of the grisms in NIC3 is itself evaluated to be in the 5%–10% range.

<sup>a</sup>  $J$ : 1.15–1.35  $\mu\text{m}$ ; 0 mag = 1576.2 Jy for  $\lambda_{\text{eff}} = 1.25$   $\mu\text{m}$ .

<sup>b</sup>  $H$ : 1.50–1.80  $\mu\text{m}$ ; 0 mag = 1018.6 Jy for  $\lambda_{\text{eff}} = 1.65$   $\mu\text{m}$ .

<sup>c</sup>  $K$ : 2.00–2.40  $\mu\text{m}$ ; 0 mag = 672.8 Jy for  $\lambda_{\text{eff}} = 2.20$   $\mu\text{m}$ .

vation dates. We measure a magnitude difference  $\Delta_K \sim 0.1$  between maximum and minimum of Pluto's light curve, which agrees with previous ground-based observations.

#### 4.2. Charon

Figure 2*b* compares the calibrated spectra of the leading and trailing hemispheres of Charon and shows that (1) water ice appears to be in its crystalline state on both hemispheres, (2) the *HST* NICMOS geometric albedo is slightly higher than reported from analysis of the mid-1980s mutual occultation events, and (3) spectral features characteristic of species such as hydrogen cyanide (HCN) or, more probably, ammonia hydrate ( $\text{NH}_3 \cdot \text{H}_2\text{O}$ ) are present in the spectrum of Charon's leading side.

##### 4.2.1. Crystalline Ice versus Amorphous

The spectra of Figure 2*b* show the  $1.65 \mu\text{m}$  spectral feature characteristic of crystalline water ice for both the trailing and leading hemispheres of the satellite. Water ice has also been found in its crystalline state on the surfaces of the large satellites of Uranus (Grundy et al. 1999). This suggests that resurfacing processes can occur in the outer solar system at a faster rate than required for water ice to turn into its amorphous state under the action of solar irradiation (Strazzulla et al. 1992). A possible mechanism, proposed by Brown & Calvin (2000), implicates vaporization of the outermost layers of water ice on Charon by micrometeorite bombardments and recondensation of this ice into its crystalline state over the surface of the satellite. Figure 2*b* also shows differences between the spectral response of Charon's leading and trailing hemispheres. In particular, the spectral slope at short wavelengths is stronger for the leading side, which could be directly linked to the nature of the neutral absorber in surface. Also, the depth of the  $1.55 \mu\text{m}$  water band is shallower for the leading side, which might indicate hemispheric variations in the grain size distribution of water ice, although we would expect a similar behavior for the  $2.02 \mu\text{m}$  water band. The  $2.21 \mu\text{m}$  feature in the spectrum of Charon's leading side will be discussed below in § 4.2.3.

##### 4.2.2. Geometric Albedo of Charon

Table 3 presents the broadband photometric measurements derived from the spectra of Charon's trailing and leading sides. The *K*-band magnitude difference between the hemispheres is within the uncertainty of our measurements, confirming that the leading and trailing sides of Charon have a similar brightness. The calibration of our *HST* NICMOS spectra returns a value for Charon's geometric albedo of  $p \sim 0.42 \pm 0.05$  in the  $1.8 \mu\text{m}$  water continuum region (Fig. 2*b*), which is slightly higher than the  $p \sim 0.34 \pm 0.05$  measurement (Roush et al. 1996) derived from the mid-1980s mutual events (although both error bars overlap). The difference in Charon's geometric albedo reported in this paper is small, but larger than the uncertainty of the NICMOS grism calibration. The latter is estimated to be a few percent higher than the 5%–10% range reported by Freudling & Pirzkal (1998), mainly because of the processes applied to our data to separate the contributions of Pluto and Charon. Furthermore, the good agreement between the NICMOS determination of Pluto's geometric albedo (Fig. 2*a*) and earlier ground-based measurements supports the absolute calibration of our data. This sensibly higher determination of Charon's albedo

cannot be produced by residual contamination from the planet. Indeed, the immediate consequence would be to underestimate Pluto's albedo, whereas our measurements agree with the ground-based results. The slightly higher NICMOS albedo is consistent (within the error bars) with the earlier results and might simply reflect larger uncertainties than previously estimated in Charon's diameter and in the photometric calibration of the mutual-event data.

Nevertheless, we cannot entirely rule out the possibility that the differences measured in the albedos of Pluto and Charon could result from systematic errors in the radiometric calibration returned by the NICMOSlook package. If the increase in albedo is real, then it might suggest time-variable phenomena over Charon, such as seasonal changes occurring while the system is moving away from the Sun. Also, the satellite is now observed with an aspect angle  $10^\circ$  larger than during the 1987 mutual events, presenting a slightly larger apparent cross section of its southern polar region. The present geometry could contribute to an increase in albedo if the southern polar region is made of material that exhibits a high reflectivity at these wavelengths. Comparison with other icy satellites of the outer solar system is possible. Near-infrared spectroscopy of the large satellites of Saturn returns geometric albedo measurements in the range  $p \sim 0.2$  (Hyperion) to  $p \sim 1.0$  (Mimas). The NICMOS observations show that Charon's albedo of  $p \sim 0.4$  at  $1.8 \mu\text{m}$  is very similar to the albedo of Iapetus's trailing side, which is typical of a "dirty ice" composition. Figure 3 shows the result of modeling the reflectance spectra of Charon's leading and trailing hemispheres with an intimate mixture ( $\sim 90\%$ ) of crystalline water ice (Grundy & Schmitt 1998) and  $\sim 10\%$  of a spectrally blue component, the latter being required to match the continuum level at short wavelengths. In this model, the water ice is made of  $30 \mu\text{m}$  grains while the blue component corresponds to  $10 \mu\text{m}$  particles having a reflectance spectrum decreasing linearly from 8% to 6% over the  $1.0$ – $2.7 \mu\text{m}$  region. Both spectra of Charon are reasonably well matched by the spectrum of pure water ice, except for the  $2.21 \mu\text{m}$  band and the short-wavelength region (Charon's trailing side). The modeling results do not require the addition of  $\text{CO}_2$  ice or  $\text{CH}_4$  ice to improve the final fit.

##### 4.2.3. The Leading Hemisphere of Charon

The *HST* NICMOS spectrum of Charon's leading side (Fig. 3*b*) is identical to the spectrum of the same side of the satellite obtained at Keck by Brown & Calvin (2000). It displays the same  $2.21 \mu\text{m}$  spectral feature that was attributed to the presence of ammonia hydrate on the surface of the satellite. This additional and independent detection of the  $2.21 \mu\text{m}$  band suggests that this spectral feature is real and rules out the possibility that it could be produced by residual contamination from Pluto.

The first obvious candidate for this  $2.21 \mu\text{m}$  feature is  $\text{CH}_4$  ice itself. Although we do not expect methane ice to still be present over Charon's surface, we nevertheless modeled the spectrum of Charon's leading side (Fig. 4) with an intimate mixture of water ice ( $\sim 78\%$ ;  $30 \mu\text{m}$  grain size), methane ice ( $\sim 15\%$ ;  $30 \mu\text{m}$  grain size), and  $\sim 7\%$  of the spectrally blue compound described above. The model presented in Figure 4 shows that adding methane ice to the mixture does not provide a good match to the features observed in the spectrum of Charon's leading side. The small amounts of methane used in the model can reproduce

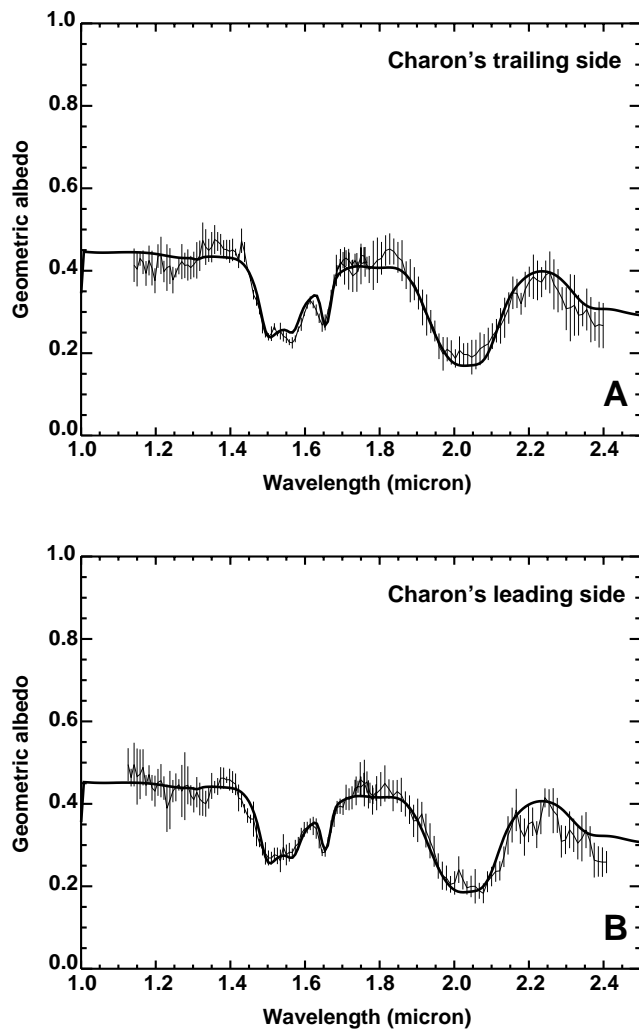


FIG. 3.—Hapke modeling of the spectra of the (a) trailing and (b) leading hemispheres of Charon using an intimate mixture of water ice (40 K) and a blue component (<10%) to adjust the continuum. The best matches are obtained for water ice grain sizes of  $\sim 30 \mu\text{m}$ . The  $\pm 1\sigma$  error bars plotted with the spectra correspond to the standard deviation of the spectral data set (residual scatter) after calibration and division by the spectrum of a solar analog. Deviations of the spectra from the models show that the surface composition of Charon is probably more complex than pure water ice.

the depth of the  $2.21 \mu\text{m}$  feature while allowing the two-band complex in the  $1.7\text{--}1.8 \mu\text{m}$  region to be at the noise level of the spectrum. However, further comparison shows that (1) the deeper bands of methane longward of  $2.3 \mu\text{m}$  are too strong to match our data set and (2) the  $2.2 \mu\text{m}$  band of methane is too narrow to provide a good fit to the  $2.21 \mu\text{m}$  feature.

Other possible candidates display an absorption feature near  $2.2 \mu\text{m}$ . Figure 5 shows the reflectance spectra of ammonia hydrate for different weight concentrations of  $\text{NH}_3$ , as well as the spectrum of hydrogen cyanide. Based only on their respective “history” of detections, HCN would be a stronger candidate than  $\text{NH}_3$ . Indeed, ammonia ice has never been securely detected on any other satellite of the solar system, while HCN has been found several times in cometary material, as well as in some star-forming regions. In addition, HCN has a sublimation temperature of 87 K and can be trapped in water ice quite efficiently, to be released solely by evaporation of the water ice (Notesco &

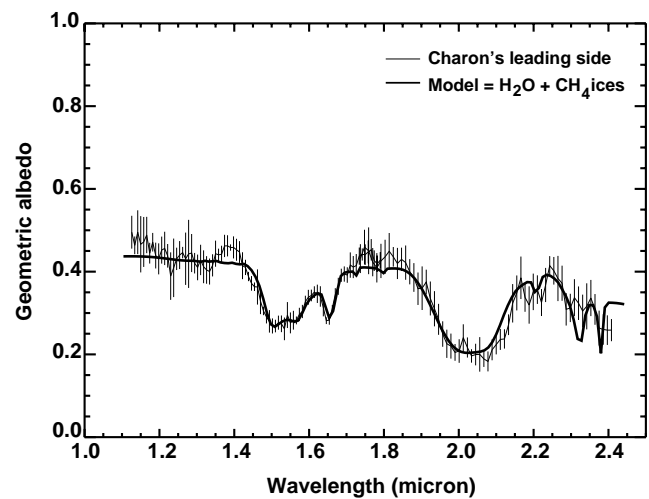


FIG. 4.—Modeling of the spectrum of Charon's leading side with an intimate mixture of water and methane ices. While the model fits nicely the depth of the  $2.21 \mu\text{m}$  feature, the methane bands longward of  $2.3 \mu\text{m}$  are too deep to fit our data set, ruling out the possibility that methane ice is the compound responsible for the  $2.21 \mu\text{m}$  band observed in the spectrum of Charon's leading side. The optical constants for methane ice were obtained at 30 K by R. H. Brown & V. Anicich (1997, unpublished).

Bar-Nun 1997). On the other hand, near-infrared spectra of Europa's trailing side (Brown et al. 1988) recorded in 1980 and 1985 showed several bands at  $1.8$ ,  $2.21$ , and  $2.32 \mu\text{m}$  that were associated with ammonia ice. The same absorption features could not be detected in subsequent observations of Europa obtained in 1986, suggesting that, if real, the presence of ammonia on Europa had to be associated with transient phenomena occurring at the surface of the satellite. Such events are supported by high spatial resolution images of the satellite obtained with the *Galileo* spacecraft, which showed distinct surface features that could be produced by the sublimation of volatiles such as ammonia ice (Greeley et al. 1998). Figure 6 shows a comparison of the reflectance spectra of HCN and  $\text{NH}_3 \cdot \text{H}_2\text{O}$  (3% ammonia) with the spectra of the trailing and leading hemispheres of Charon. Although other absorption features are present in our spectrum of Charon's leading side (e.g., a dip at  $1.77 \mu\text{m}$  and a marginal feature at  $2.3 \mu\text{m}$ ), only the band at  $2.21 \mu\text{m}$  clearly emerges above the noise level of our data. We will note that, except for the  $2.21 \mu\text{m}$  band, HCN and  $\text{NH}_3$  have most of their absorptions coinciding with the strong bands of water ice, making their detection particularly difficult. We will therefore limit our discussion to the  $2.2 \mu\text{m}$  region of the spectrum. Figure 6 shows also that  $\text{NH}_3$  displays a narrower absorption at  $2.21 \mu\text{m}$  than HCN, better matching the feature observed in the spectrum of Charon's leading side. For this reason, we consider ammonia hydrate a better candidate than HCN to explain the  $2.21 \mu\text{m}$  band, although higher S/N spectra are needed to definitively identify the compound responsible for this absorption. It is also important to note that the relatively poor match of the  $2.21 \mu\text{m}$  feature is mainly due to the lack of optical constants for ammonia hydrate. When these data are available, it will be possible to estimate what type of ammonia mixture is present on Charon and whether pure  $\text{NH}_3$  coexists with ammonia hydrate (Brown & Calvin 2000). Also, the profile of the  $2.21 \mu\text{m}$  feature in our model is probably affected by the fact that the spectra of HCN and

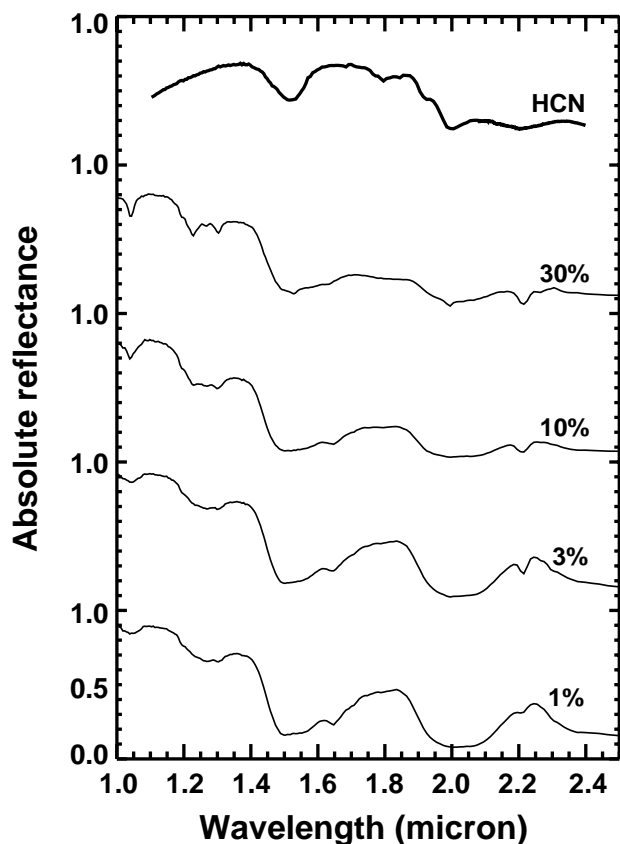


FIG. 5.—Reflectance spectra of possible candidates for the 2.21  $\mu\text{m}$  absorption feature. The uppermost spectrum is of an anhydrous HCN polymer (Cruikshank et al. 1991), while the four others are of a mixture of water ice (crystalline) and ammonia ice for weight abundances of 1%, 3%, 10%, and 30% of  $\text{NH}_3$  (Brown et al. 1988). Note the increasing depth of the strong ammonia band at 2.21  $\mu\text{m}$  with increasing amounts of ammonia ice in the  $\text{NH}_3 \cdot \text{H}_2\text{O}$  mixture.

$\text{NH}_3 \cdot \text{H}_2\text{O}$  were obtained at temperatures (room temperature for HCN, 77 K for  $\text{NH}_3 \cdot \text{H}_2\text{O}$ ) different from Charon's surface temperature ( $\sim 40$  K). Finally, despite the fact that the detection of an absorption feature near 2.3  $\mu\text{m}$  is more marginal than that of the strongest 2.21  $\mu\text{m}$  band, it could correspond to a similar absorption detected in the spectrum of the trailing side of Europa (Brown et al. 1988), which was attributed to the presence of ammonia hydrate in surface.

#### 4.3. Ammonia Hydrate on Charon: Possible Origins

Several cases can be discussed in which compounds (other than water ice) present on Charon's leading side are either endogenic or exogenic. Geological activity such as cryovolcanism, producing a flow of pristine volatile material through cracks, could transport interior ices to the surface of the satellite. Charon's surface cannot have retained any volatiles over the age of the solar system, but nitrogen ice could still be present below the external layer. Such a mechanism would be possible only if ammonia were produced from nitrogen at a faster rate than needed for the volatiles to sublimate, but even in this case, the apparent concentration of ammonia ice on the leading side of Charon would remain to be explained. Also, any tidal heating of Charon that could be responsible for a volcanic-type activity similar to Triton's is suspected to have stopped long ago, given that Pluto and Charon are both rotationally locked

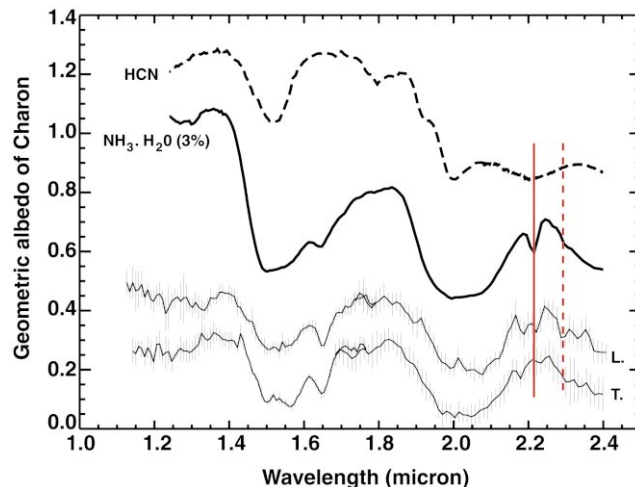


FIG. 6.—Comparison of the band positions between the spectra of HCN and  $\text{NH}_3 \cdot \text{H}_2\text{O}$  (3% ammonia) and the calibrated spectra of Charon's leading (L) and trailing (T) hemispheres. The spectrum of the trailing side has been shifted downward by 0.15 units while the reflectance spectra of HCN and  $\text{NH}_3 \cdot \text{H}_2\text{O}$  are overplotted with respective offsets of 0.35 and 0.6 units. The solid vertical line marks the position of the 2.21  $\mu\text{m}$  band visible only in the spectrum of Charon's leading side. Both  $\text{NH}_3$  and HCN display an absorption at 2.21  $\mu\text{m}$  similar to the absorption present in the spectrum of Charon's leading side, but the profile of the ammonia hydrate band matches better the 2.21  $\mu\text{m}$  feature than does HCN. The marginal 2.3  $\mu\text{m}$  absorption in the spectrum of Charon's leading side could correspond to a shallower band in the spectrum of ammonia hydrate (dashed line), but spectra with better S/N are needed in order to clearly identify the species responsible for the absorptions observed in the spectrum of Charon's leading side.

and tidally relaxed. Alternatively, new species can be produced on Charon from bombardment of its surface by ions escaping from Pluto. Owen et al. (1993) estimated that  $\text{N}_2$  constituted more than 99% of Pluto's atmosphere. Given Pluto's nitrogen-rich surface and atmosphere, the escape of  $\text{N}_2$  is likely to happen simultaneously with the escape of  $\text{CH}_4$ . The escape rate of  $\text{N}_2$  is driven by both the atmospheric temperature ( $\sim 106$  K; Yelle & Lunine 1989) and the  $\text{CH}_4$  mixing ratio, and it varies seasonally with the heliocentric distance of Pluto. The 9.8 eV energy level required to dissociate molecular nitrogen (Allen 1973, p. 47) corresponds to the regime of ionizing extreme-UV radiation, with wavelengths shorter than 1260 Å. This energy range contains the intense Ly $\alpha$  emission line ( $\lambda = 1216$  Å) of the solar chromosphere, which produces a flux of  $3.4 \times 10^{12}$  photons  $\text{m}^{-2} \text{s}^{-1}$  at 30 AU from the Sun and can dissociate molecular nitrogen into  $\text{N}^+$  ions ( $\text{N}_2^+$  recombines rapidly). The simplest mechanism to form ammonia on one side of the satellite would be to have  $\text{N}_2/\text{N}^+$  escaping from Pluto's atmosphere and impacting the leading side of Charon because of its orbital motion. Whipple, Trafton, & Stern (1989) showed that a portion of the molecules escaping from Pluto's atmosphere would be trapped in the Pluto-Charon system, similar to the interaction occurring in the case of a close binary star system. Compositional differences between leading and trailing hemispheres of satellites have already been observed in our solar system and usually implicate hemispheric resurfacing by redeposition of dust or ice released by a nearby body. The dark leading hemisphere of Iapetus is a good illustration of resurfacing processes implicating the action of an external source, in this case, the nearby satellites Hyperion (Buratti et al. 1999) and Phoebe.

The nature of the plasma surrounding Charon is mainly controlled by the existence (or absence) of a magnetosphere around Pluto, which is driven by both the degree of magnetization of the planet and its atmospheric escape rate. If Pluto maintains a weak remnant magnetization (comparable to chondrite meteorites), the interaction of escaping ions from Pluto's atmosphere with the weak solar wind at 30 AU would produce a magnetosphere extending beyond the orbit of Charon (Bagenal et al. 1997). The plasma surrounding Charon would then be controlled by ions escaping from the planet. However, with the locked system defined by Pluto, its magnetic field, and Charon, it is not clear that such a mechanism would favor the accumulation of ions over the leading hemisphere of the satellite.

Is the production of  $\text{NH}_3$  from bombardment of water ice with  $\text{N}^+$  likely to happen? Laboratory experiments to measure the effect of ion irradiation of an icy surface (Strazzulla 1998) show that the implantation of reactive ions over the surface of planetary satellites could produce new molecular species that are not native to those surfaces. However, Strazzulla & Palumbo (1998) also showed that bombardment of a mixture of water and ammonia ices by energetic ions decreases the concentration of ammonia ice. In addition, the binding energy of  $\text{NH}_3$  is 2.2 times smaller than that of  $\text{N}_2$ , and it is therefore photolytically destroyed quite rapidly. An estimate of its production and dissociation rates is needed to test whether ammonia ice can be preserved from rapid dissociation. If ammonia ice is present on Charon, it is probably formed as ammonia clathrate, and  $\text{H}_2\text{O}$  molecules could provide some shielding once the upper layers were depleted of  $\text{NH}_3$ . Indeed, small amounts

of organics, which are excellent UV absorbers, mixed with the water ice on Charon, would still allow the detection of the  $\text{NH}_3$  bands in the near-infrared while providing shielding to protect  $\text{NH}_3$  from rapid dissociation.

Much work still needs to be done in order to better understand the complex nature of Charon's surface. Additional spectra at higher spectral and spatial resolution will help to securely identify the compound or compounds responsible for the absorption features observed in the spectrum of its leading side. Further observations at different rotational phases of the satellite will allow us to measure the spatial distribution of species other than water ice and to test whether the  $2.21 \mu\text{m}$  feature is also present in the spectrum of the Pluto-facing hemisphere of Charon. Also, laboratory experiments to measure the optical properties of  $\text{NH}_3$  ice need to be carried out to model the recent spectra of Charon obtained from the ground and space, and the effect of bombardment of water ice by  $\text{N}^+/\text{N}_2$  should be studied in more detail to quantify the effectiveness of this process to form ammonia hydrate on Charon.

The authors would like to thank Rodger Thompson and Marcia Rieke from the NICMOS Instrument Definition Team, and Wolfram Freudling and Norbert Pirzkal from ST-ECF for the support provided with NICMOSlook. We are also grateful to Tobias Owen for his helpful comments on the manuscript, and Dale Cruikshank for providing the reflectance spectrum of HCN. This work was performed at the Jet Propulsion Laboratory, California Institute of Technology, under contract to the National Aeronautics and Space Administration.

#### REFERENCES

- Allen, C. W. 1973, *Astrophysical Quantities* (3d ed.; London: Athlone)
- Bagenal, F., Cravens, T. E., Luhmann, J. G., McNutt, R. L., & Cheng, A. F. 1997, in *Pluto and Charon*, ed. S. A. Stern & D. J. Tholen (Tucson: Univ. Arizona Press), 523
- Brown, M. E., & Calvin, W. M. 2000, *Science*, 287, 107
- Brown, R. H., Cruikshank, D. P., Tokunaga, A. T., Smith, R. G., & Clark, R. N. 1988, *Icarus*, 74, 262
- Buie, M. W., Cruikshank, D. P., Lebofsky, L. A., & Tedesco, E. F. 1987, *Nature*, 329, 522
- Buie, M. W., & Fink, U. 1987, *Icarus*, 70, 483
- Buie, M. W., & Grundy, W. M. 2000, *Icarus*, 148, 324
- Buie, M. W., Tholen, D. J., & Horne, K. 1992, *Icarus*, 97, 211
- Buratti, B. J., Hicks, M. D., Tryka, K. A., Sittig, M., & Newburn, R., Jr. 1999, *BAAS*, 31, 1093
- Cruikshank, D. P., Allamandola, L. J., Hartmann, W. K., Tholen, D. J., Brown, R. H., Matthews, C. N., & Bell, J. F. 1991, *Icarus*, 94, 345
- Cruikshank, D. P., Pilcher, C. B., & Morrison, D. 1976, *Science*, 194, 835
- Cruikshank, D. P., Roush, T. L., Moore, J. F., Sykes, M., Owen, T. C., Bartholomew, M. J., Brown, R. H., & Tryka, K. A. 1997, in *Pluto and Charon*, ed. S. A. Stern & D. J. Tholen (Tucson: Univ. Arizona Press), 221
- Davies, M. E., et al. 1995, *Celest. Mech. Dyn. Astron.*, 63, 127
- Douté, S., Schmitt, B., Quirico, E., Owen, T. C., Cruikshank, D. P., de Bergh, C., Geballe, T. R., & Roush, T. L. 1999, *Icarus*, 142, 421
- Dumas, C., Terrile, R. J., Brown, R. H., & the NICMOS IDT. 1999, in *Pluto and Triton: Comparison and Evolution over Time Conference Abstracts* (Flagstaff: Lowell Obs.)
- Fink, U., & DiSanti, M. A. 1988, *AJ*, 95, 229
- Freudling, W., & Pirzkal, N. 1998, in *NICMOS and the VLT*, ed. W. Freudling & R. Hook (Garching: ESO), 47
- Greeley, R., et al. 1998, *Icarus*, 135, 4
- Grundy, W. M., Buie, M. W., Stansberry, J. A., Spencer, J. R., & Schmitt, B. 1999, *Icarus*, 142, 536
- Grundy, W. M., & Schmitt, B. 1998, *J. Geophys. Res.*, 103, 25809
- Jewitt, D. C. 1994, *AJ*, 107, 372
- Labs, D., & Neckel, H. 1968, *Z. Astrophys.*, 69, 1
- Lauer, T. R. 1999, *PASP*, 111, 1434
- Lellouch, E., Laureijs, R., Schmidt, B., Quirico, E., de Bergh, C., Crovisier, J., & Coustenis, A. 2000, *Icarus*, 147, 220
- Marcialis, R. L., Rieke, G. H., & Lebofsky, L. A. 1987, *Science*, 237, 1349
- McCarthy, P. J., et al. 1999, *ApJ*, 520, 548
- Notesco, G., & Bar-Nun, A. 1997, *Icarus*, 126, 336
- Owen, T. C., et al. 1993, *Science*, 261, 745
- Park, S. K., & Schowengerdt, R. A. 1983, *Comput. Vision Graphics Image Processing*, 23, 256
- Pirzkal, N., & Freudling, W. 1998, in *NICMOS and the VLT*, ed. W. Freudling & R. Hook (Garching: ESO), 55
- Reinsch, E. M., Burwitz, V., & Festou, M. C. 1994, *Icarus*, 108, 209
- Roush, T. L. 1994, *Icarus*, 108, 243
- Roush, T. L., Cruikshank, D. P., Pollack, J. B., Young, E. F., & Bartholomew, M. J. 1996, *Icarus*, 119, 214
- Stern, S. A., Buie, M. W., & Trafton, L. M. 1997, *AJ*, 113, 827
- Stern, S. A., Trafton, L. M., & Gladstone, G. R. 1988, *Icarus*, 75, 485
- Strazzulla, G. 1998, in *Solar System Ices*, ed. B. Schmitt, C. de Bergh, & M. Festou (Dordrecht: Kluwer), 281
- Strazzulla, G., Baratta, G. A., Leto, G., & Foti, G. 1992, *Europhys. Lett.*, 18, 517
- Strazzulla, G., & Palumbo, M. E. 1998, *Planet. Space Sci.*, 46, 1339
- Thekekar, M. P. 1973, *Sol. Energy*, 14, 109
- Thompson, R. I., Rieke, M., Schneider, G., Hines, D. C., & Corbin, M. 1998, *ApJ*, 492, L95
- Tryka, K. A., Brown, R. H., Cruikshank, D. P., Owen, T. C., Geballe, T. R., & de Bergh, C. 1994, *Icarus*, 112, 513
- Whipple, A. L., Trafton, L. M., & Stern, S. A. 1989, *BAAS*, 21, 982
- Yelle, R. V., & Lunine, J. I. 1989, *Nature*, 339, 288
- Young, E. F., Galdamez, K., Buie, M. W., Binzel, R. P., & Tholen, D. J. 1999, *AJ*, 117, 1063
- Young, L. A., Elliot, J. L., Tokunaga, A., de Bergh, C., & Owen, T. 1997, *Icarus*, 127, 258